Physics of Plasmas

RESEARCH ARTICLE | APRIL 04 2024

Investigation of high field plasma dynamics in a laser-produced plasma expanding into a background gas

Z. K. White ; K. G. Xu ; S. Chakraborty Thakur

Phys. Plasmas 31, 042105 (2024)
https://doi.org/10.1063/5.0193271

AIP Publishing

Investigation of high field plasma dynamics in a laser-produced plasma expanding into a background gas

Cite as: Phys. Plasmas **31**, 042105 (2024); doi: 10.1063/5.0193271
Submitted: 21 December 2023 · Accepted: 21 February 2024 ·
Published Online: 4 April 2024

Z. K. White,[1,a)] K. G. Xu,[1] and S. Chakraborty Thakur[2]

AFFILIATIONS

[1]Mechanical and Aerospace Engineering Department, University of Alabama in Huntsville, Huntsville, Alabama 35899, USA
[2]Physics Department, Auburn University, Auburn, Alabama 36849, USA

[a)]Author to whom correspondence should be addressed: zw0015@uah.edu

ABSTRACT

This paper presents an overview of experimental results of a laser-produced plasma expanding into a background gas, immersed within a large range of highly uniform magnetic fields (of up to 3 T), that are transverse to the expanding plasma. We used intensified gated imaging to capture the expansion of the plasma across and along the magnetic field lines to observe the spatiotemporal expansion dynamics for different magnetic field strengths. We observe changes in the perpendicular and parallel dynamics of the laser-produced plasmas expansion at high magnetic field. In addition, our results have also indicated the presence of electron-ion hybrid instabilities at relatively high pressures (100 mTorr) and relatively high magnetic field strengths (2 T), in accordance with theoretical calculations.

I. INTRODUCTION

The interaction of a moderately dense, highly transient plasma with an external magnetic field is an interesting problem in plasma physics with applications to astrophysical phenomena,[1–5] magnetic confinement fusion,[6–9] and pulsed plasma propulsion systems.[10–14] Studying this phenomenon gives insight into the conversion of kinetic energy into thermal energy, shockwaves,[15–22] confinement of the particles in an external magnetic field,[23,24] and onset of instabilities[25,26] in a transient plasma system. To create plasma such as these, it is common to ablate a solid surface using a nanosecond pulse laser.[27–30] Previous work has defined the expansion dynamics,[31–33] confinement,[6,34] and instability onset[35,36] in a broad range of targets (aluminum, carbon), laser energies (10 mJ–30 J), magnetic field configurations (uniform, non-uniform), and magnetic field strengths (0–1.5 T). Additional experimentation into different regimes of collisionality and magnetization of the plasma could give insight into the phenomena listed above.

Instabilities are commonly observed in laser-produced plasmas; the usual instabilities present in these plasmas are generally categorized as magnetic Rayleigh–Taylor instabilities (RTIs).[25,26,37,38] Others have proposed the existence of another instability driven by shear from electron motion called the electron-ion hybrid instability (EIH),[35,39–41] but for the most part, this instability has only been experimentally considered in relatively low magnetic field cases. Another feature of laser-produced plasma flows interacting with external magnetic fields is the stagnation distance. Understanding how far a plasma will expand against a background magnetic field is important in proposed pulsed plasma propulsion systems.[42,43] Estimating the stagnation distance, commonly referred to as the critical radius, has been done for a range of magnetic field strengths,[6,34] but how the bubble radius is affected over a wide increase in magnetic field has been sparsely researched.[44]

The aim of the current study was a parametric investigation of magnetization and collisionality on plasma expansion. We have found evidence of the electron-ion hybrid instability up to 2 T, which is damped with higher background pressures. Additionally, we have observed the convergence of the critical radius with one-dimensional (1D) approximation of the initial energy by extrapolating the kinetic energy of the plasma.

II. EXPERIMENTAL METHODS

To complete the parametric study, we aimed for a high field (∼3 T), high pressure environment (50–300 mTorr). In our experiment, we utilize the superconducting magnet at Auburn University, the Magnetized Dusty Plasma Experiment (MDPX) device. MDPX is a split-bore, magnet system that houses four superconducting magnets in a cylindrical cryostat that has an overall axial dimension of 157 cm

and an outer diameter of 122 cm. The system features a 50 cm diameter "warm bore" where experimental hardware can be placed. In the configuration used for this study, the primary MDPX octagonal vacuum chamber was mounted into the bore of the magnet. For the purpose of this study, the key experimental feature is that the evacuated target region is placed in the center of the MDPX device at a location where a highly uniform (i.e., less than 1% axial or radial ripple) magnetic field up to 4 T can be produced. Additional details of the MDPX device configuration are given in previously published works.[45–48]

The plasma was created by ablating a small 1 mm diameter cylindrical carbon fiber rod using an Nd:YAG laser focused to a spot size approximately the diameter of the rod. The laser was operated at 532 nm and focused onto the target by a 150 mm lens. The laser energy was set at a constant 275-mJ energy with a pulse width of 6 ns to provide a laser fluence of 3.5 GW/cm^2. To avoid repeatedly ablating a single spot on the rod, a Thorlabs kinetic mounted mirror was placed between the laser and the testing area. The kinetic mirror mount allowed us to change the height of the laser spot along the carbon rod by pitching the angle of the beam up and down. Rods were periodically replaced when the entire length was ablated. The rod was mounted within a plastic 3D printed holder that was then placed in a vacuum chamber located in the bore of the MDPX device. The magnetic fields used in this study were 0.125, 0.25, 0.5, 1, 1.5, 2, 2.5, and 3 T. The vacuum chamber within the bore was a hexagonal chamber with an inner diameter of ∼35 cm with a height of 18 cm. A simple schematic of the experimental setup is shown in Fig. 1. The vacuum chamber was pumped by a turbomolecular pump to a base pressure of ∼5 mTorr. Needle valves and mass flow controllers were used to provide background argon up to the desired pressures within the chamber.

To observe the plasma expansion, gated optical imaging was obtained using an Andor iStar 334T ICCD camera. The gated images were synchronized with the laser pulse to measure the emission of the plasma expansion at different delays to gather a complete picture of the expansion. The gate width of the ICCD was set to 5 ns for each shot. The ICCD was positioned both perpendicular and parallel relative to the magnetic field lines, as seen in Figs. 1(a) and 1(b). At lower applied magnetic field strengths of less than 1 T, we were able to obtain a spatial resolution of 0.05 mm/pixel, but at field strengths above 1 T, the resolution decreased to 0.1 mm/pixel as the camera had to be moved further away. Additionally, the high field directly above the bore of the superconducting magnet limited the amount of data obtained parallel to the magnetic field lines.

Figure 2 gives a representative example of how the plasma is oriented throughout the remainder of the paper. The images obtained in the Fig. 1(a) configuration correspond to Fig. 2(a), and the configuration in Fig. 1(b) corresponds to the expansion orientation shown in Fig. 2(b). The targets are centered at [0,0] throughout the remainder of the paper. The images were transferred as 16-bit data files into MATLAB where they were postprocessed to obtain the desired information. The postprocessing consisted of assuming negligible emission far away from the plasma to set a threshold on the image using the average of the top row of the CCD array. This value was taken at approximately $y = -20$ mm. Any index values that fell below this value were then set to zero.

ICCD images were obtained for the plasma expansion in 5 ns intervals ranging from 5 to 1000 ns with a single laser shot corresponding to a single ICCD acquisition. The images captured a line-of-sight

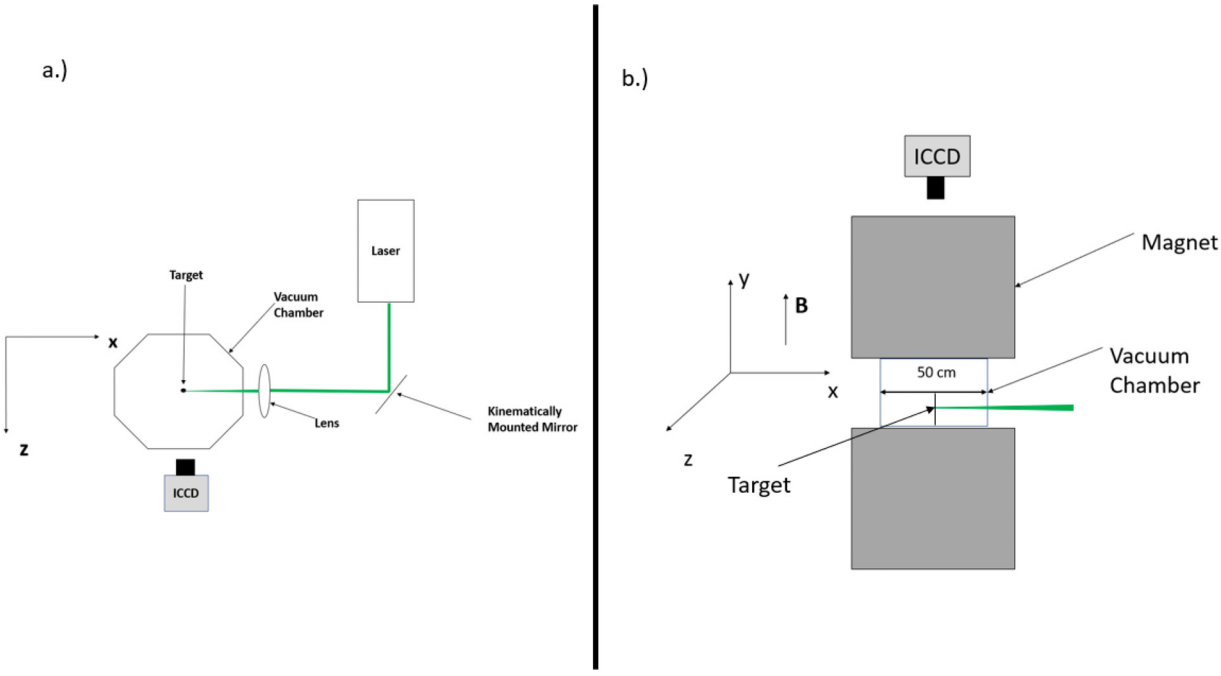

FIG. 1. Experimental setup in the MDPX device. A pulsed Nd:YAG is fired at a carbon rod that is oriented parallel to the magnetic field. Images of the plasma expansion were taken in two separate configurations. The first configuration (a) was the camera imaging the plane perpendicular to the magnetic field, and the second (b) was the camera imaging the plane-parallel to the magentic field. The orientation of the magnetic field is in the +y direction, as shown above.

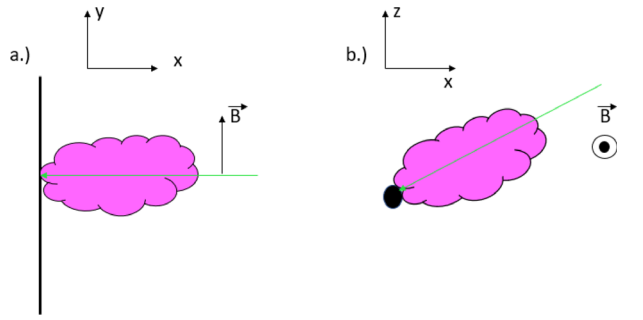

FIG. 2. Sketches how the ICCD imaged the plasma expansion at both (a) the first (xy-plane) and (b) second (xz-plane) configurations.

broadband emission of the plasma expansion. The velocity of the plasma was approximated by combining all the delayed images and selecting emission values at specific distances away from the target to create temporal profiles of the plasma emission. Using these temporal profiles at multiple locations along the x-axis, the peaks of the profiles were used as approximations of the bulk plasma passing that point. Once the time of arrival at multiple points is known, an approximation of the plasma velocity can be made, and this velocity is helpful in defining the approximate magnetization of the plasma through defining the β value. Throughout the work, there will be cases where multiple peaks are present, and in these cases, the first peak was taken to signify the bulk plasma.

III. RESULTS

A. Approximation of β values

In the quickly moving expansion of a laser-produced plasma, the balance between the dynamic pressure of the plasma and the magnetic pressure of the external field allows us to discern the degree of diamagnetism of the plasma. This equilibrium parameter is referred to as the β value of the plasma. Having a β greater than unity suggests that the plasma can sufficiently "push" the external magnetic field out of its way. At lower β, we can expect the magnetic field to diffuse quickly into the expanding plasma and the plasma to be trapped along the magnetic field lines. The equation below can be used to calculate the total β:

$$\beta = \frac{n_e k T_e + \frac{1}{2}\rho V^2}{\frac{B^2}{\mu_0}}, \tag{1}$$

where n_e is the number density, k is the Boltzmann's constant, T_e is the temperature, ρ is the mass density, V is the expansion velocity, B is the external magnetic field, and μ_0 is the magnetic permeability of the plasma. To understand how these dynamics worked in our experiments, we found it important to measure β as a function of the magnetic field strength. First, some high-level assumptions are made to make these measurements possible. For the electron density and temperature, we used the measurements taken by Harilal *et al.*[49] as baseline values for our approximation as their target plasma and laser fluence were at similar values as ours. In addition to Harilal *et al.*, the work of others[44,50] has shown that the presence of the magnetic field had a negligible effect on the electron density, but the temperature increased due to heating of the plasma attributed to adiabatic compression and Joule heating. The values used for our approximation are shown in Table I.

TABLE I. Values used for β calculation.

B (T)	n_e (#/m^3)	T_e (eV)	V (m/s)	Upper bound β	Lower bound β
0.125	1×10^{22} to 1×10^{23}	1.82	34 000	1464.71	146.471
0.25	1×10^{22} to 1×10^{23}	1.82	250 00	204.6854	20.468 54
0.5	1×10^{22} to 1×10^{23}	1.82	19 800	33.45 895	3.345 895
0.75	1×10^{22} to 1×10^{23}	1.82	15 000	9.226 027	0.922 603
1	1×10^{22} to 1×10^{23}	1.82	13 700	4.480 452	0.448 045
1.5	1×10^{22} to 1×10^{23}	1.82	6250	0.735 707	0.073 571
2	1×10^{22} to 1×10^{23}	1.82	4400	0.320 209	0.032 021
2.5	1×10^{22} to 1×10^{23}	1.82	4250	0.200 988	0.020 099
3	1×10^{22} to 1×10^{23}	1.82	3450	0.126 565	0.012 656

Using the indexed data after postprocessing in MATLAB, we were able to obtain line-of-sight images of the plasma expansion. Figures 3(a) and 3(c) show example images from the plasma expansion at 500 ns, 0 T at 300 and 200 mTorr, respectively. The red lines placed at 2 and 4 mm indicate where intensity measurements were taken. For the different time step images, the intensity at each position along the centerline (y = 0) was determined and used to produce the intensity vs time graphs, as shown in Figs. 3(c) and 3(d). Each time interval was captured in a single laser pulse, so multiple laser shots make up a single temporal profile. The plasma expansion velocity is then calculated from the distance and time between the peaks at each location. The velocities calculated are also shown in Table I, and the results of this β approximation can be seen in Fig. 4.

Figure 3(b) is the time evolution of the plasma at 300 mTorr and 0 T along the y = 0 axis at two different x locations: x = 2 and 4 mm. A notable feature visible in each of the curves at the different locations is a multiple peak feature. At the 2 mm location, the first peak occurs ~70 ns after the laser pulse then oscillates to around 120 ns before a sharp drop to no emission. Then, after the emission goes to zero, the next phase of the emission crosses along the measurement point. This second wave of emission carries along a much longer emission profile over the measured 500 ns. The 4 mm location shows a similar initial fast peak, but with a larger time delay between the initial peak and secondary peak. The separate peaks suggest that there are distinct populations of particles at separate velocities. These "fast" and "slow" particles could be the result of a collisional shock wave commonly referred to as a blast wave,[36] causing a secondary shock wave to reflect through the interior of the plasma.[19,20]

Figure 3(d) shows the time evolution of the emission at a background pressure of 100 mTorr and magnetic field strength of 0 T at x = 2 and 4 mm. The emissions at 2 mm begin at nearly the same time as at the higher 300 mTorr pressure, but within the first wave of emissions, there is only a single peak unlike the oscillatory behavior observed at the higher pressure. Additionally, the second peak appears much faster than at 300 mTorr. The 4 mm temporal profile at 200 mTorr differs largely from 300 mTorr with the absence of two distinct peaks in emissions; the lack of a double-peaked structure here

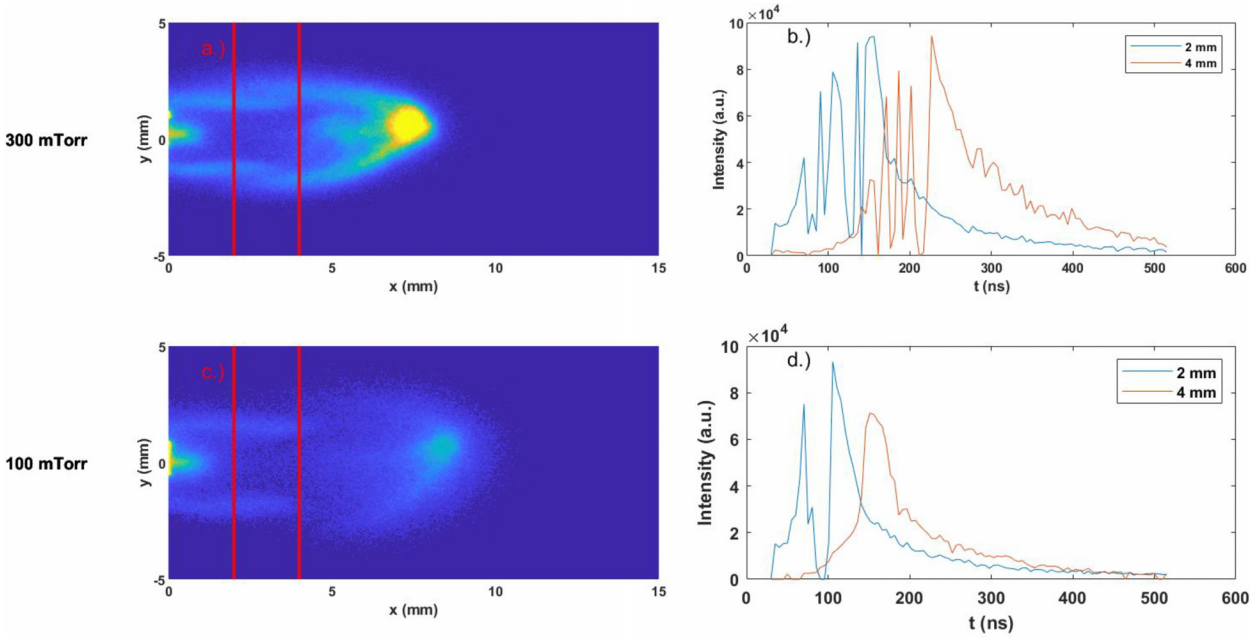

FIG. 3. (a) The expansion of a plasma into no magnetic field at 300 mTorr where the red lines depict the x locations that the temporal profiles shown in (b). The same phenomena are shown for the 100 mTorr case in (c) and (d).

suggests that the blast wave seen in the higher-pressure cases is no longer causing a reflecting back through the plasma due to the lack of collisions. The collisionality is estimated as the ratio between λ_{mfp} and the calculated critical radius, R_c. λ_{mfp} is the mean free path between ion-neutral collisions and estimated by the following equation:

$$\lambda_{mfp} = \frac{1}{n\sigma}, \tag{2}$$

where n is the neutral gas density and σ is the argon cross section. The estimate from this calculation of λ_{mfp}/R_c supports that the plasma

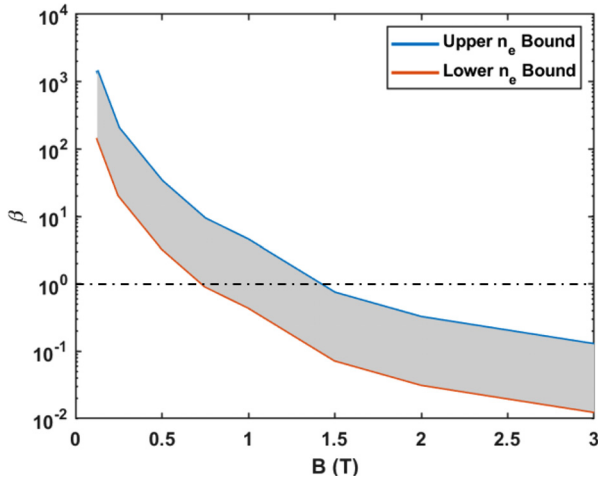

FIG. 4. Estimation of the range of β values. Put dash line for unity value. The dashed line represents the β = 1 point.

should be collisional at both pressures with values of collisionality calculated to be 0.1167 at 300 mTorr and 0.51 at 100 mTorr.

B. Effect of magnetic field and pressure on plume structure

Figures 5(a)–5(c) show the expansion in the x-z plane, as in configuration 2 in Fig. 1(b), at 100 mTorr and 2 T at 100, 150, and 200 ns after the laser pulse. Additional images were not able to be obtained at other magnetic field strengths because of complications with the camera interacting with the strong field above the bore of the superconducting magnet. Even with this limitation, we were able to obtain data that illuminated the transition of a smooth plasma front to one indicating possible instability onset. The initial image in Fig. 5(a) shows the expansion of the plasma at 100 ns with the direction of expansion indicated by Fig. 2(b). Here, we see the smooth front along the axis of motion. In Fig. 5(b), the plasma expansion is shown at 150 ns after the laser pulse, and small perturbations along the plasma front become evident. At the final time of 200 ns in Fig. 5(c), we then see full onset and splitting and the formation of a "lobe" or a separated plasma region at the top of the image. Images taken shown in Figs. 5(d)–5(f) with no B field present showed no evidence of any of the perturbations along the plasma front. Comparing this to the imaging in the x-y plane at 2 T in Fig. 5(g)–5(i), we see that the non-homogeneity seen in Fig. 5(c) corresponds to Fig. 5(i) that has no signs of the splitting.

Additionally, Fig. 6 shows the effect of increasing pressure on the splitting structures observed along the plasma front. In Fig. 6, the top row images show the plasma expansion at 2 T and 200 ns, but as the pressure is increased, the observed structures become less pronounced. To check the degree of collisionality empirically, the temporal profiles of each expansion associated with the specific pressure are shown on

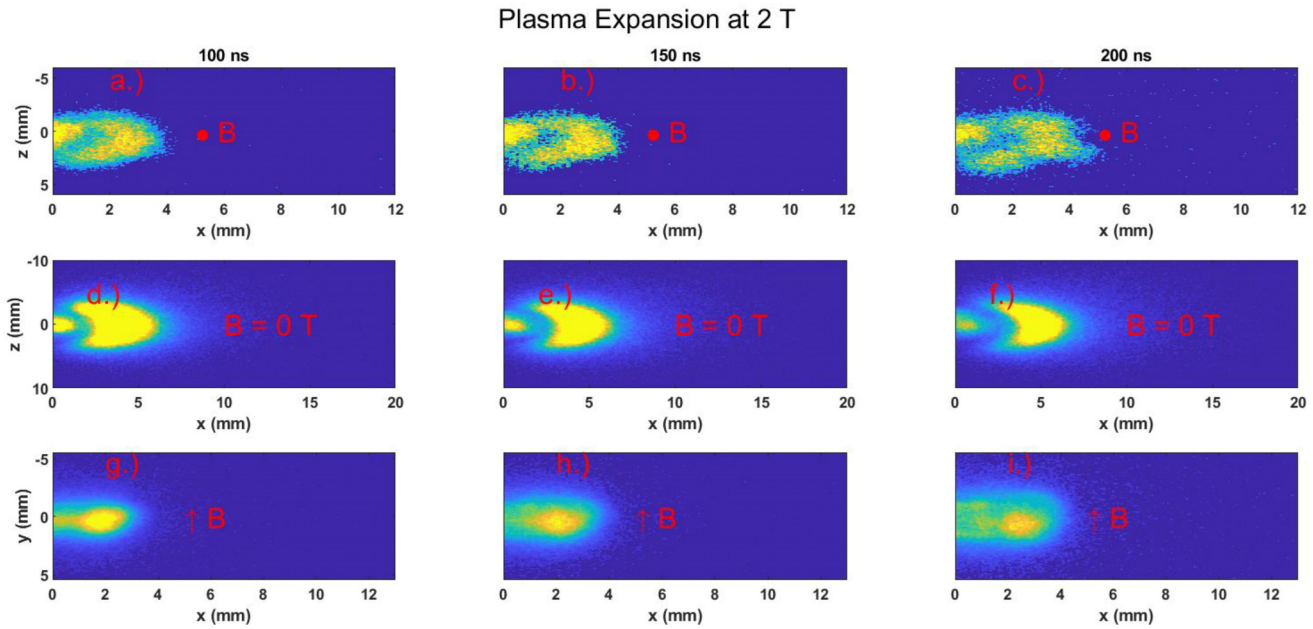

FIG. 5. The expansion of the plasma in the x-z plane with B = 2 T (a)–(c) and no B (d)–(f), and x-y planes at B = 2 T (g)–(i). In the xz plane images, one can clearly see plume splitting occurring in the plasma expansion at the 200 ns time step. In the xy plane images, no clear evidence is observed.

the bottom row. As stated earlier, spatial resolution was sacrificed to obtain images at the higher magnetic field strengths. Because of this, the images in the bottom row of Fig. 6 show the expansion at 1 T, the highest available field at the 0.025 mm/pixel resolution. The double peak structure is present in both the 200 and 300 mTorr cases suggesting collisionality but is not present at 100 mTorr, suggesting that the plasma may be in a non-collisional regime at this pressure. Quantitatively, the collisionality of the three were 0.25, 0.5, and 1.4 for the 300, 200, and 100 mTorr cases, respectively, indicating that a transition from collisionless to collisional behavior could be expected.

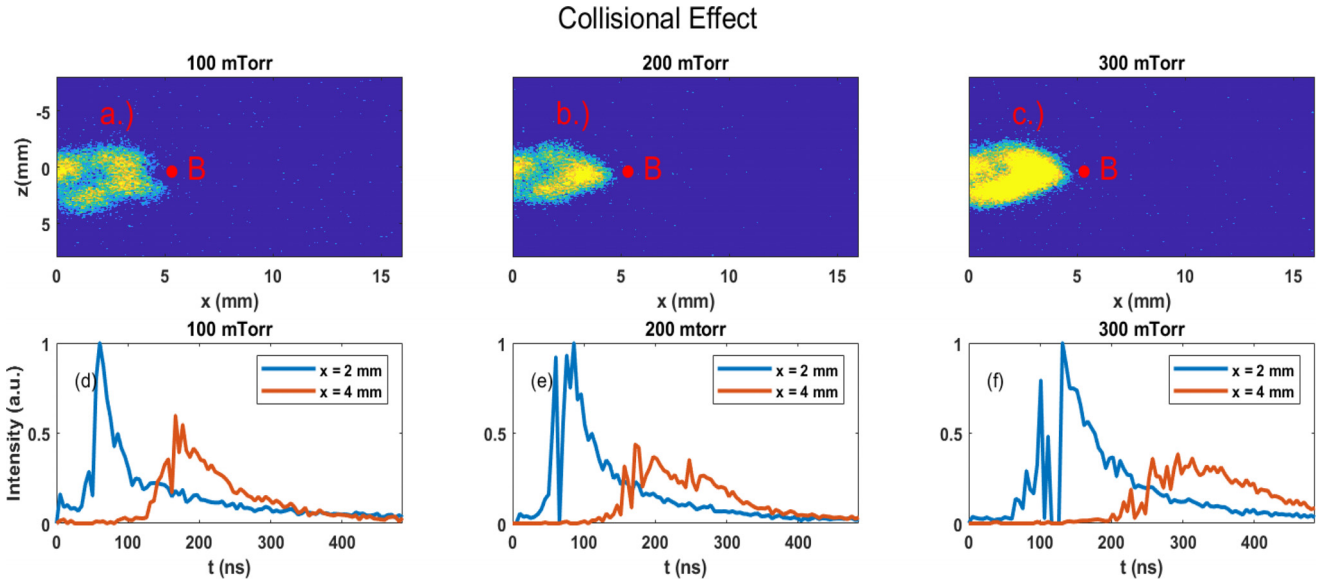

FIG. 6. The effect of increasing pressure on the plume splitting at 2 T (a)–(c) and the transtion from a collisionless plasma at 1 T exhibiting no shock waves (d) to a collisional plasma with the existence of a shock indicated by the two large double peaks (e) and (f).

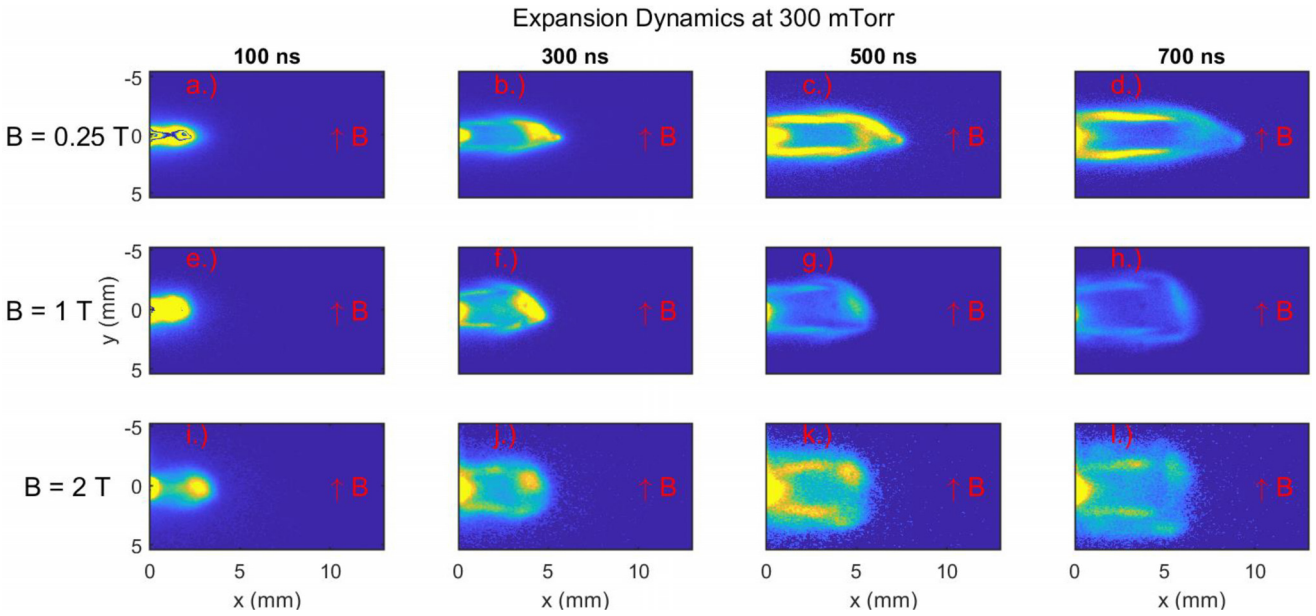

FIG. 7. Temporal images of the plasma at B = 0.25 T (a)–(d), B = 1 T (e)–(h), and B = 2 T (i)–(l) for the 300 mTorr background pressure case. The dynamics of the plasma expansion such as the sharp leading edge and depth of propagation into the x-direction are altered considerably by the increased magnetic field. Still, no evidence of instability is seen in the imaging of the xy plane.

C. Expansion dynamics at $\beta > 1$, $\beta \sim 1$, and $\beta < 1$

The next result shows the effect of magnetic field on the expansion dynamics. All images shown will be of the x-y plane since only the 2 T case was imaged in the x-z plane. Figure 7 shows the plasma expansion at 300 mTorr for 0.25 T (top row), 1 T (middle row), and 2 T (bottom row). The figure shows that as the magnetic field is increased, many features of the expanding plasma are changed. The main features observed are the sharp regions along the leading edge of the plasma scene in Figs. 7(b), 7(c), 7(f), and 7(g), the artificial cavity region created between the plume and the target region, and the contraction of the plasma in the x-direction. First, as the magnetic field is increased along the 300 ns column in Figs. 7(b), 7(f), and 7(j), the sharp region is blunted, which suggests that the plasma is transitioning into a more magnetized regime. The magnetization here is estimated by the ratio between the directed ion Larmor radius and critical radius of the plasma plume. For the three magnetic field strengths given below and using the calculated bulk velocities, the approximate magnetization of the three cases is 1.06, 0.35, and 0.05, respectively. The other features also undergo slight changes in the collisional case. For example, the artificial cavity region that is formed by the expanding plasma plume and the bright stationary plasma region near the target elongates along the y-axis as the field is increased, and the expected contraction of the plasma expansion also occurs which will be discussed in Sec. III D.

D. Critical radius as a function of magnetic field magnitude

External magnetic fields can effectively confine the expansion of plasmas. The plasma expansion at 0.25 T shows that the plasma penetrates across the magnetic field much more than at 1 T. Because of these consistent observations across all our magnetic field strengths, we wanted to correlate our observed plasma expansion across the magnetic field (positive x-direction) with previously defined theoretical frameworks. A common way to estimate the plasma expansion is the bubble radius. The bubble radius is an ideal magnetic confinement radius of a plasma defined by when the velocity of the plasma comes to zero. We used the bubble radius calculation to understand how the dynamics of expansion changed when transitioning the plasma from a diamagnetic to nondiamagnetic regime. The bubble radius is calculated from the one-dimensional energy balance between the kinetic energy of the plasma and the magnetic energy of the field. The energy components in the plasma are defined as

$$E_0 = \frac{1}{2} m V^2 + \frac{B^2}{2\mu_0}\left(\frac{4}{3}\pi R^3\right), \tag{3}$$

where m is the mass density of the plasma, V is the plasma velocity, μ_0 is the magnetic permeability, E_0 is the total energy of the plasma, and R is the radius. In the limit where the plasma velocity goes to zero, one can obtain the bubble radius of an expanding spherical plasma with

$$R_b = \left(\frac{3\mu_0 E_0}{2\pi B^2}\right)^{\frac{1}{3}}. \tag{4}$$

The assumption here is that the plasma expansion is spherical. To check the validity of using the spherical radius assumption, we calculate the plasma radius in the direction of expansion. Figure 8 shows the results of this comparison. The theory line follows Eq. (4) with the assumption that only half of the energy input by the laser beam is transferred directly into the initial energy of the plasma. This assumption has been commonly used throughout the literature.[29,33,36] The other lines depict the measured radius in the x-direction of the plasma expansion in our

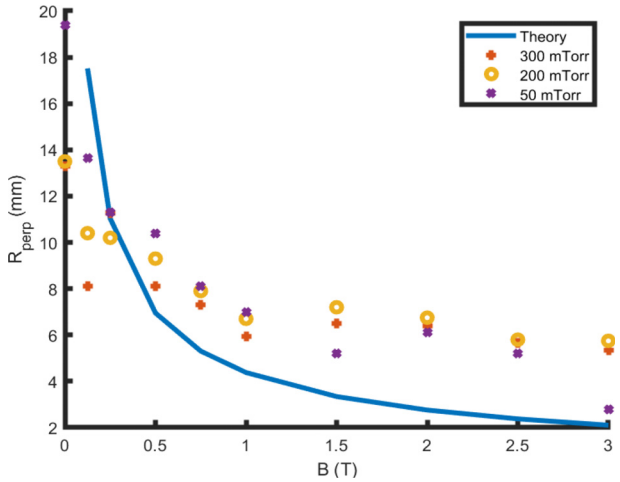

FIG. 8. The measured critical radii (penetration of the plasma in the x-direction) at multiple pressures and magnetic fields. Only loose agreement between the measured values and the theoretical value is obtained.

experiments at a time delay of t = 1000 ns for 300, 200, and 50 mTorr pressure. Our critical radius measurements are taken from the surface of the carbon fiber rod out to where the intensity signal drops to approximately the same level as the background. While there is no exact agreement with the theory, the results are generally within a factor of 3 or 4, with the 50 mTorr case being the closest. There is also a leveling off of the radius for 50 mTorr when the magnetic field strength reaches 1.5 T. The critical radii at lower magnetic fields (<0.75 T) show the largest difference between the three pressures. As the magnetic field is increased, the radius of the 50 mTorr cases decreases while the 300 and 200 mTorr begin to provide similar results.

IV. DISCUSSION

A. Instability onset

In Fig. 5(c), the plasma plume undergoes a splitting into three separate lobes. We believe this plume splitting was due to the electron-ion hybrid instability. Generally, plume splitting can arise from the classic Rayleigh–Taylor instability from the ambient lighter gas supporting the heavier laser plasma, a class of magnetic Rayleigh–Taylor instabilities predicted and observed throughout many studies,[25,36,38] or other predicted instabilities driven by the shear from electron motion such as the electron-ion hybrid instability.

The hydrodynamic RTI occurs when the deceleration of the plasma is primarily because of collisions with the background medium. Because of the importance of collisions, the hydrodynamic RTI should not occur when collisions between the background gas and laser plasma are negligible. From our results, we see that the plume splitting is present primarily at the 100 mTorr case, but less so when the pressure is increased to 200 and 300 mTorr. Once again noting that when the mean free path is much smaller than the scale length of the plasma, we can consider the plasma to be collisional, the 200 and 300 mTorr cases can be expected to experience collisions while the 100 mTorr case may be considered collisionless. It is noteworthy to mention that the comparison between Figs. 5 and 6(d)–6(f) is not exact because of the difference in the magnetic field strengths, but nothing from the image suggests the onset of collisional behavior. Additionally, the increased magnetic field would have no effect on the background neutral argon atoms, but we have not considered the effect of photoionization of background particles in this study. Therefore, the lack of collisional behavior observed at 100 mTorr eliminates the hydrodynamic RTI as an option.

The magnetic Rayleigh–Taylor instability classes we will focus on initially are magnetohydrodynamic (MHD) and large Larmor radius (LLR) instabilities. The MHD RTI is driven by gravitational forces that drive drifts of the ions and electrons in opposite directions, which then grow the instability through the induced E × B drift from the charge separation. The LLR RTI is driven by the charge separation arising from unmagnetized ions. The E × B drift then only affects the electrons driving the instability even more. The MHD RTI can be defined as a regime where the ion Lamor radius, ρ_i is much smaller than the scale of the critical radius, $\rho_i \ll R_b$ and the LLR RTI is the regime where $\rho_i \gg R_b$ where ρ_i is the ion directed Larmor radius. Both instabilities are predicted to be stabilized by finite Larmor radius (FLR) effects when the Larmor radius is on the same order of the characteristic scale length.[38] In the context of our experiments, magnetic RTI of the LLR form was not expected because $\rho_i \ll R_b$ at the shown 2 T magnetic field. In contrast to this, the MHD RTI could have very well been present and cause for the splitting. Growth rates of the MHD RTI are given as

$$\gamma_{RT} \sim \left(\frac{g_{eff}}{L_n}\right)^{\frac{1}{2}}, \tag{5}$$

where g_{eff} is the effective deceleration from the magnetic field, L_n is the density scale length, and the onset time is estimated by

$$\tau_{RT} = \frac{2\pi}{\gamma_{RT}}. \tag{6}$$

The g_{eff} was estimated by $g_{eff} = \frac{d^2x}{dt^2}$ of the equation shown in Fig. 9 and the estimated density scale length to be on the order of our critical

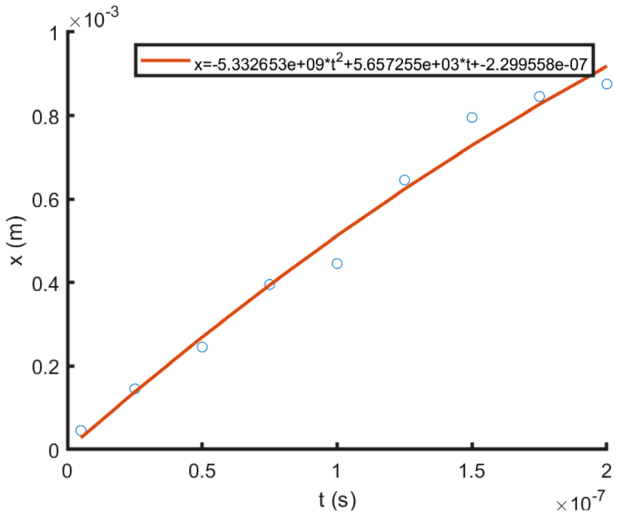

FIG. 9. Position vs time plot of the plasma expansion at 2 T with trendline. The equation for the trendline was used to approximate the effective deceleration of the plasma for the MHD RTI instability.

radius (~1 mm). The g_{eff} calculated was $\sim 1.6 \times 10^{10}$ m/s^2 which corresponds to an onset time of approximately 2000 ns which is much too large for the observed appearing of the splitting.

Both the hydrodynamic and magnetic RTI seem to not fit the onset of the plume splitting; therefore, we then looked to define what could be driving the onset of plume splitting in the imaging parallel (x-z plane) to the magnetic field from shear-driven instabilities. Peyser *et al.*[35] and Behera *et al.*[44] have both observed a shear-driven instability occurring in laser-produced plasmas at similar laser irradiance ranges as used in the current study. The primary velocity shear-driven instability identified is the electron-ion hybrid instability, which follows the following growth rate $\gamma \sim 0.01\omega_{LH}$ where the ω_{LH} is the lower hybrid frequency given by

$$\omega_{LH} = \frac{\omega_{pi}\Omega_e}{\sqrt{\omega_{pe}^2 + \Omega_e^2}}, \tag{7}$$

and the time of onset can be approximated by

$$\tau = \frac{2\pi}{0.01\omega_{LH}}, \tag{8}$$

where ω_{pi} is the ion plasma frequency, ω_{pe} is the electron plasma frequency, and Ω_e is the electron cyclotron frequency. The approximation of the 100th of the lower hybrid frequency was found by following the analysis given by Ganguli *et al.*[39] from the following normalized dispersion relation given by

$$\left(\frac{d^2}{d\bar{x}^2} - \tilde{k}_y^2 + F(\tilde{\omega})\frac{f''(\bar{x})}{\tilde{\omega} - f(\bar{x})}\right)\phi(\bar{x}) = 0, \tag{9}$$

where

$$F(\tilde{\omega}) = \frac{\delta^2}{(\delta^2+1)\left[1 - \left(\frac{\beta}{\tilde{\omega}}\right)^2\right]},$$

$$\beta = \sqrt{\frac{1}{\mu\alpha^2\tilde{k}_y^2\left(1+\frac{1}{\delta^2}\right)}},$$

$$\alpha \approx \frac{V}{L\omega_e},$$

$$f(x) = \sec^2(x),$$

where μ is the ion/electron mass ratio, α is the shear parameter, δ is the ratio between the electron plasma frequency and electron cyclotron frequency, and $\tilde{k}_y$ is the normalized wave number. The shear parameter is approximated as the maximum plasma velocity divided by the shear scale length and the electron cyclotron frequency. The shear scale is estimated as close in size to our laser spot size of 1 mm. The results of the lower-hybrid normalized growth rates from the solution of Eq. (9) at different shear parameters at the B = 2 T case and the $n_e = 10^{23}$ m^{-3} are shown in Fig. 10.

Taking these equations and calculating the onset time derived from the plasma parameters in our experiment, we find that an onset time of approximately 175 ns is more apt for our plasma expanding in a 2 T field. At 100 mTorr, we observe the features of the instability appearing near 150 ns, which is in good agreement with the electron-ion hybrid onset time compared to RTI. Additionally, the theory behind the growth rate estimation assumes unmagnetized ions while

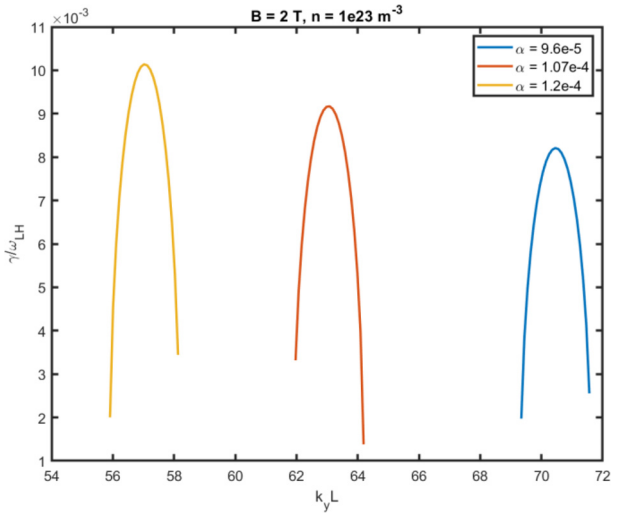

FIG. 10. Electron-ion hybrid growth rate approximated from the differential equation for the dispersion relation.

all the ions cannot be assumed to be completely unmagnetized in our experiments at 2 T. Furthermore, a local approximation was made to analytically solve Eq. (9), and the α value was approximated loosely with consideration given to the maximum measured plasma velocity and the shear scale length. We do not observe any obvious signs of instability formation in the x-y plane, and this is important to note because previous experiments[29,40,51,52] have shown the existence of flute instabilities within the diamagnetic regime. Particularly, there were instabilities observed along the surface of the plasma at magnetic field strengths well below 0.5 T, but our results indicate there is no onset of instabilities until well above 1 T. It is important to note that in Ref. 36 the laser energies (30 J), plasma target (aluminum), and background pressures (<0.1 mTorr) were different than our experiment. Specifically, it was found that the visibility of the instabilities could be significantly enhanced by an increase in laser energy, but with the limitations of our setup, no energies above 270 mJ were attempted. Other attempts[35] with closer laser energies (150 mJ), but different targets (aluminum) and background pressures (1×10^{-6} Torr) have shown similar results to ours with more visible instabilities at lower magnetic field strengths. The difference here is that it has been conjectured that RTI are dampened by collisions which would be abundant in our relatively high-pressure experiments, and also, the large onset times of >1 μs of the electron-ion hybrid instability at the lower magnetic fields. Collisions also seemed to significantly affect the appearance of the electron-ion hybrid instability we believe we have observed in our study. For example, in Fig. 6, we show a comparison between the plasma at 100 and 300 mTorr. Each of the data points is taken at 200 ns into the expansion of the plasma which is similar to the calculated onset time from Eq. (7).

B. Comparison of experimental bubble radius to energy balance calculations

The validity of the bubble radius theory at higher magnetic fields has not been deeply investigated; here, we have shown good agreement between the experimentally measured radii and the calculated value

from a simple energy balance between the kinetic and magnetic energies of the system. We notice that in Fig. 8 that the theory line and the experimental data are loosely correlated and have more agreement at 50 mTorr. We believe that this could be because of multiple reasons. First, the expansion of laser-produced plasma from a solid surface expands orthogonally to the surface. Therefore, whether a cylindrical or flat surface is used, the expansion shape will not likely perfectly conform to the spherical shape assumed in the derivation of Eq. (4). It should be noted that approximating the shape of the plasma as a sphere has been used to calculate the critical radii of the plasma expansions in previous work.[44] In that work, the authors utilized multiple camera views to approximate the general shape of the plasma and then used a modified Eq. (4) to calculate the critical radius. Because of our limitations of camera views, we used the general formulation, but even with the assumption of spherical expansion, we found that at 50 mTorr the experimental results showed decent agreement.

Another source of deviation could be the estimation of the E_0 value in Eq. (3). It is likely that the assumption of the total energy coupled from the laser pulse into the expanding plasma has been underestimated in our energy balance. On the other hand, many losses have not been accounted for such as thermal conduction, instabilities, and radiation. Based on the significant change in the critical radii at 200 and 300 mTorr, it is likely that increased coupling with the energy of the expanding plasma with the background gas because of collisions could lead to the deviation from the value calculated from the energy balance at the lower fields. Because of the overshoot of the experimental bubble radius at magnetic fields greater than 0.5 T, we are not sure that measuring the broadband emission provides the clearest view of the bubble radius.

C. Summary

In summary, we have observed evidence of electron-ion hybrid instabilities in the high B limit of the current theory. Extensions of this work could focus on both the characterization of the diamagnetic cavity and compare the dynamics of the diamagnetic cavity with the propagation of the shockwaves and the onset of instabilities. Furthermore, increased resolution imaging in the xz plane at an increased number of magnetic field strengths and pressures would be insightful into the behavior of the plume splitting.

ACKNOWLEDGMENTS

This work was supported by a NASA Space Technology Research Fellowship (No. 80NSSC191144). This work was also supported by DOE Frontiers in Plasma Science (No. DE-SC0021280) and by the NSF EPSCoR RII-Track-1 Cooperative Agreement No. OIA-1655280.

Additionally, I would like to thank Dr. Chris Crabtree, Dr. Ami Dubois, and Dr. Guru Ganguli for helpful discussions on the theory of electron-ion hybrid instabilities.

AUTHOR DECLARATIONS

Conflict of Interest

The authors have no conflicts to disclose.

Author Contributions

Z. White: Conceptualization (lead); Data curation (lead); Formal analysis (lead); Investigation (lead); Methodology (lead); Writing – original draft (lead). **K. G. Xu:** Conceptualization (supporting); Methodology (supporting); Supervision (lead); Writing – review & editing (equal). **S. Chakraborty Thakur:** Conceptualization (supporting); Methodology (supporting); Supervision (supporting); Writing – review & editing (equal).

DATA AVAILABILITY

The data that support the findings of this study are available from the corresponding author upon reasonable request.

REFERENCES

[1]P. V. Heuer, M. S. Weidl, R. S. Dorst, D. B. Schaeffer, S. K. P. Tripathi, S. Vincena, C. G. Constantin, C. Niemann, and D. Winske, Phys. Plasmas **27**, 042103 (2020).
[2]R. P. Drake, Phys. Plasmas **7**, 4690 (2000).
[3]C. Niemann, W. Gekelman, C. G. Constantin, E. T. Everson, D. B. Schaeffer, A. S. Bondarenko, S. E. Clark, D. Winske, S. Vincena, B. Van Compernolle, and P. Pribyl, Geophys. Res. Lett. **41**, 7413, https://doi.org/10.1002/2014GL061820 (2014).
[4]D. B. Schaeffer, W. Fox, D. Haberberger, G. Fiksel, A. Bhattacharjee, D. H. Barnak, S. X. Hu, and K. Germaschewski, Phys. Rev. Lett. **119**, 025001 (2017).
[5]K. Burdonov, R. Bonito, T. Giannini, N. Aidakina, C. Argiroffi, J. Beárd, S. N. Chen, A. Ciardi, V. Ginzburg, K. Gubskiy, V. Gundorin, M. Gushchin, A. Kochetkov, S. Korobkov, A. Kuzmin, A. Kuznetsov, S. Pikuz, G. Revet, S. Ryazantsev, A. Shaykin, I. Shaykin, A. Soloviev, M. Starodubtsev, A. Strikovskiy, W. Yao, I. Yakovlev, R. Zemskov, I. Zudin, E. Khazanov, S. Orlando, and J. Fuchs, Astron. Astrophys. **648**, A81 (2021).
[6]S. S. Harilal, M. S. Tillack, B. O'Shay, C. V. Bindhu, and F. Najmabadu, Phys. Rev. E **69**, 026413 (2004).
[7]A. Kumar, V. Chaudhari, K. Patel, S. George, S. Sunil, R. K. Singh, and R. Singh, Rev. Sci. Instrum. **80**, 033503 (2009).
[8]A. Kumar, H. C. Joshi, V. Prahlad, and R. K. Singh, Phys. Lett. A **374**, 2555 (2010).
[9]A. Huber, U. Samm, B. Schweer, and P. Mertens, Plasma Phys. Controlled Fusion **47**, 409 (2005).
[10]G. Statham, S. White, R. B. Adams, Y. C. F. Thio, R. Alexander, S. Fincher, A. Philips, and T. Polsgrove, in *39th AIAA/ASME/SAE/ASEE Joint Propulsion Conference & Exhibit*, 2003.
[11]J. Cassibry, R. Cortez, M. Stanic, W. Seidler, R. Adams, G. Statham, and L. Fabisinski, in *48th AIAA/ASME/SAE/ASEE Joint Propulsion Conference & Exhibit*, 2012.
[12]R. B. Adams, J. Cassibry, D. Bradley, L. Fabisinski, and G. Statham, in *50th AIAA/ASME/SAE/ASEE Joint Propulsion Conference*, 2014.
[13]A. Maeno, T. Hinaga, N. Yamamoto, A. Sunahara, S. Fujioka, and H. Nakasima, J. Propuls. Power **30**, 54 (2014).
[14]R. Kawashima, T. Morita, N. Yamamoto, N. Saito, S. Fujioka, H. Nishimura, H. Matsukuma, A. Sunahara, Y. Mori, T. Johzaki, and H. Nakashima, Plasma Fusion Res. **11**, 3406012 (2016).
[15]S. J. Langendorf, K. C. Yates, S. C. Hsu, C. Thoma, and M. Gilmore, Phys. Rev. Lett. **121**, 185001 (2018).
[16]T. Byvank, S. J. Langendorf, C. Thoma, and S. C. Hsu, Phys. Plasmas **27**, 042302 (2020).
[17]F. Chu, A. L. Lajoie, B. D. Keenan, L. Webster, S. J. Langendorf, and M. A. Gilmore, Phys. Rev. Lett. **130**, 145101 (2023).
[18]S. S. Harilal, C. V. Bindhu, M. S. Tillack, F. Najmabadi, and A. C. Gaeris, J. Appl. Phys. **93**, 2380 (2003).
[19]S. B. Wen, X. Mao, R. Greif, and R. E. Russo, J. Appl. Phys. **101**, 023115 (2007).
[20]S. B. Wen, X. Mao, R. Greif, and R. E. Russo, J. Appl. Phys. **101**, 023114 (2007).
[21]S. S. Harilal, G. V. Miloshevsky, P. K. Diwakar, N. L. Lahaye, and A. Hassanein, Phys. Plasmas **19**, 083504 (2012).
[22]A. E. Hussein, P. K. Diwakar, S. S. Harilal, and A. Hassanein, J. Appl. Phys. **113**, 143305 (2013).
[23]C. Ducruet, N. Kornilov, C. De Julián Fernández, and D. Givord, Appl. Phys. Lett. **88**, 1 (2006).

[24]A. Neogi and R. K. Thareja, Phys. Plasmas **6**, 365 (1999).
[25]B. H. Ripin, E. A. McLean, C. K. Manka, C. Pawley, J. A. Stamper, T. A. Peyser, A. N. Mostovych, J. Grun, A. B. Hassam, and J. Huba, Phys. Rev. Lett. **59**, 2299 (1987).
[26]J. D. Huba, J. G. Lyon, and A. B. Hassam, Phys. Rev. Lett. **59**, 2971 (1987).
[27]D. K. Bhadra, Phys. Fluids **11**, 234 (1968).
[28]D. W. Koopman, Phys. Fluids **19**, 670 (1976).
[29]S. Okada, K. Sato, and T. Sekiguchi, Jpn. J. Appl. Phys., Part 1 **20**, 157 (1981).
[30]A. F. Haught, D. H. Polk, and W. J. Fader, Phys. Fluids **13**, 2842 (1970).
[31]T. Muranaka, H. Uchimura, H. Nakashima, Y. P. Zakharov, S. A. Nikitin, and A. G. Ponomarenko, Jpn. J. Appl. Phys., Part 1 **40**, 824 (2001).
[32]G. Dimonte and L. G. Wiley, Phys. Rev. Lett. **67**, 1755 (1991).
[33]A. Collette and W. Gekelman, Phys. Plasmas **18**, 055705 (2011).
[34]M. S. Tillack, S. S. Harilal, F. Najmabadi, and J. O'Shay, Inert. Fusion Sci. Appl. **2003**, 319–322 (2004).
[35]T. A. Peyser, C. K. Manka, B. H. Ripin, and G. Ganguli, Phys. Fluids B **4**, 2448 (1992).
[36]B. H. Ripin, J. D. Huba, E. A. McLean, C. K. Manka, T. Peyser, H. R. Burris, and J. Grun, Phys. Fluids B **5**, 3491 (1993).
[37]D. Winske, **2384** (1996).
[38]J. D. Huba, Phys. Plasmas **3**, 2523 (1996).
[39]G. Ganguli, Y. C. Lee, and P. J. Palmadesso, Phys. Fluids **31**, 2753 (1988).
[40]A. N. Mostovych, B. H. Ripin, and J. A. Stamper, Phys. Rev. Lett. **62**, 2837 (1989).
[41]H. Romero, G. Ganguli, Y. C. Lee, and P. J. Palmadesso, Phys. Fluids B **4**, 1708 (1992).
[42]R. B. Adams, R. A. Alexander, J. M. Chapman, S. S. Fincher, R. C. Hopkins, A. D. Philips, T. T. Polsgrove, R. J. Litchford, B. W. Patton, and G. Statham, NASA Report TP–2003–212691, 2003.
[43]R. J. Litchford, G. A. Robertson, C. W. Hawk, M. W. Turner, and S. Koelfgen, in *31st Plasmadynamics Lasers Conference*, 2000.
[44]N. Behera, R. K. Singh, V. Chaudhari, and A. Kumar, Phys. Plasmas **24**, 033511 (2017).
[45]S. Williams, S. Chakraborty Thakur, M. Menati, and E. Thomas, Phys. Plasmas **29**, 012110 (2022).
[46]E. Thomas, B. Lynch, U. Konopka, M. Menati, S. Williams, R. L. Merlino, and M. Rosenberg, Plasma Phys. Control. Fusion **62**, 014006 (2019).
[47]E. Thomas, U. Konopka, D. Artis, B. Lynch, S. Leblanc, S. Adams, R. L. Merlino, and M. Rosenberg, J. Plasma Phys. **81**, 345810206 (2015).
[48]E. Thomas, A. M. Dubois, B. Lynch, S. Adams, R. Fisher, D. Artis, S. Leblanc, U. Konopka, R. L. Merlino, and M. Rosenberg, J. Plasma Phys. **80**, 803 (2014).
[49]S. S. Harilal, C. V. Bindhu, R. C. Issac, V. P. N. Nampoori, and C. P. G. Vallabhan, J. Appl. Phys. **82**, 2140 (1997).
[50]A. Neogi and R. K. Thareja, J. Appl. Phys. **85**, 1131 (1999).
[51]S. Migliuolo, Phys. Fluids **25**, 2289 (1982).
[52]D. Winske, Phys. Fluids B **1**, 1900 (1989).